NJC

New Journal of Chemistry

rsc.li/njc

A journal for new directions in chemistry

ROYAL SOCIETY
OF CHEMISTRY
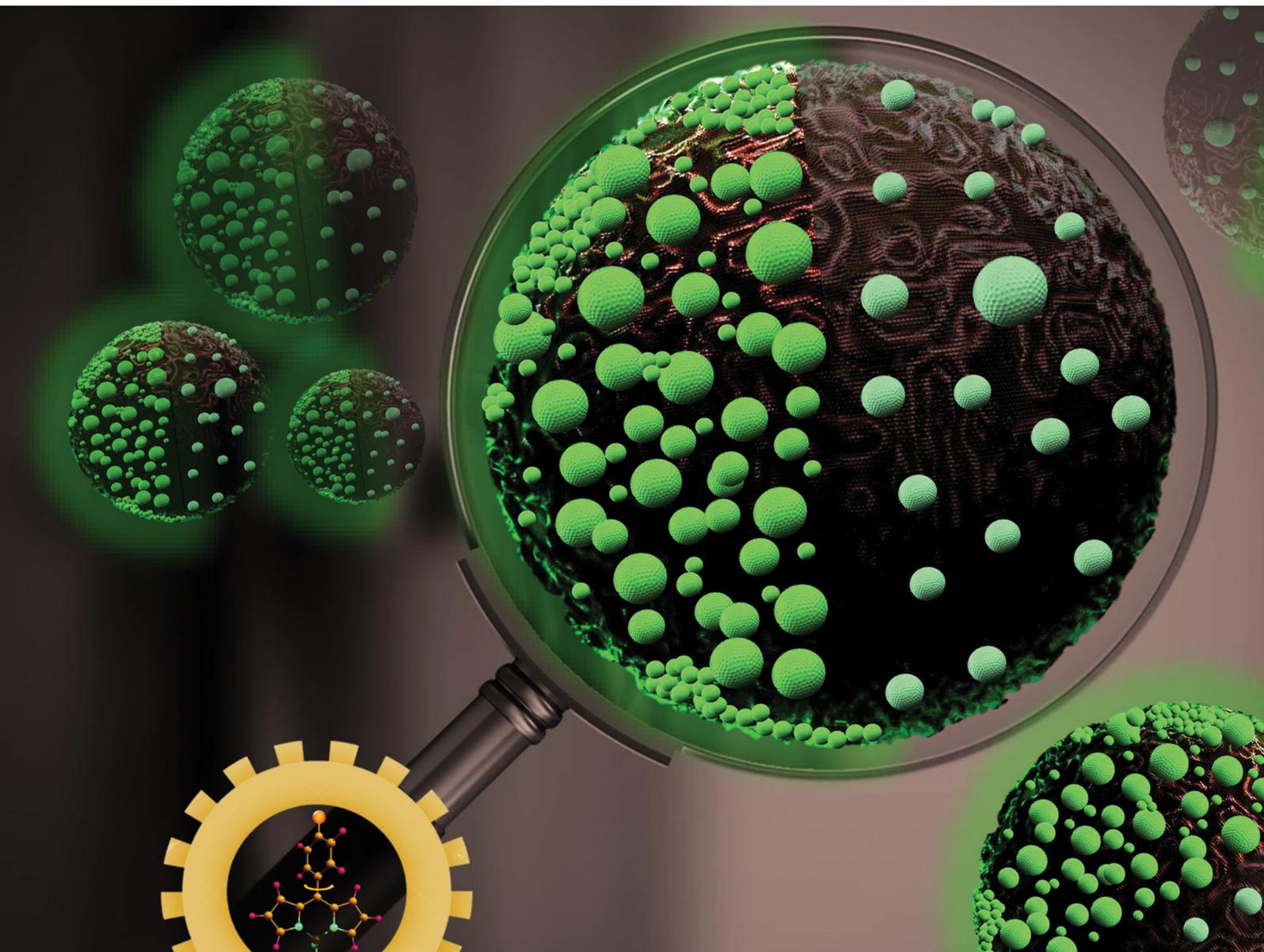
PAPER
Chinna Ayya Swamy P *et al.*
meso-Substituted BODIPY rotors as lipid droplet probes for
cell-type differentiation

CNRS

ROYAL SOCIETY
OF CHEMISTRY

Check for updates

meso-Substituted BODIPY rotors as lipid droplet probes for cell-type differentiation

Charutha Kalarikkal,[a] Anjali,[b] Koyeli Mapa*[b] and Chinna Ayya Swamy P [iD] *[a]

Cancer remains a leading cause of death worldwide despite advances in technology and therapeutics. Lipid droplets (LDs) have recently emerged as promising cancer biomarkers, as cancer cells typically exhibit a higher abundance and viscosity of LDs than normal cells. This has driven interest in developing small-molecule activatable fluorescent probes that respond to microenvironmental cues. Unlike conventional "always-on" probes, these systems enhance fluorescence response selectively in environments with altered viscosity, polarity, pH, or temperature minimizing background noise and enabling precise tracking of molecular processes within organelles. In this context, we have designed and synthesized two new BODIPY-based molecular rotors for LD targeting. The key difference between the two probes lies in their molecular conformation: compound **8** features tetramethyl groups on the indacene core, which significantly influence its optical properties. In contrast, compound **7** with more pronounced rotor dynamics shows higher sensitivity to viscosity variations. The photophysical properties are supported by DFT and TD-DFT calculations (B3LYP/6-31G(d,p), Gaussian 09W). Both probes demonstrate low cytotoxicity, good photostability, and excellent LD selectivity, allowing clear distinction between normal and cancerous cells.

1. Introduction

Globally, cancer poses a critical health challenge and continues to impede progress in life expectancy, with almost 10 million cancer-related deaths in 2020.[1,2] Despite significant advancements in medicine, early and accurate detection of cancer remains a major hurdle. Traditional diagnostic tools such as X-ray, magnetic resonance imaging (MRI), positron emission tomography (PET), and ultrasound are widely used but are often effective only at later stages of tumor development. Moreover, these methods also suffer from limitations, including exposure to harmful radiation, high costs, and low sensitivity. In recent years, fluorescence imaging has gained attention as a promising alternative, offering high specificity, real-time visualization, and minimal invasiveness, with strong potential for early detection of cancer cells.[3] However, the complexity and heterogenity of cancer at the cellular level continue to challenge current diagnostic methods.

Recently, lipid droplets (LDs) have emerged as potential cancer biomarkers due to their pivotal roles in metabolic

pathways related to cancer cell proliferation, metastasis, progression, and chemoresistance.[4–6] LDs are dynamic organelles composed of a core of neutral lipids encapsulated in a phospholipid monolayer embedded with specific proteins.[7,8] Beyond serving as lipid storage sites, LDs regulate key cellular processes such as energy homeostasis, stress regulation, protein storage, degradation, and trafficking.[5,9] Furthermore, dysfunction of LDs can result in diseases such as atherosclerosis, cardiovascular diseases, fatty liver disease and cancer.[8,10] Cancer cells typically possess higher number and larger size of LDs to meet their metabolic demands.[6,11] These characteristics provide a valuable basis for distinguishing cancerous cells from normal cells, enabling early diagnosis and targeted therapy. Although several LD-targeted fluorescent probes such as Nile red, BODIPY, and flavone derivatives have been developed,[12–18] they often suffer from drawbacks like poor selectivity, off-target staining, low photostability, cytotoxicity, and high background fluorescence.

In recent years, small-molecule activatable fluorescent probes responsive to the subcellular microenvironment have emerged as powerful tools for biological imaging and disease diagnosis. This is largely because many cellular processes are regulated by local physicochemical factors, where even subtle changes can lead to disease onset.[19–22] Among the various microenvironmental factors, viscosity plays a particularly crucial role. It governs key cellular activities such as macromolecular diffusion, intracellular transport, signal transduction, and metabolic waste removal.[23–25] Aberrant changes in viscosity have been closely associated with

[a] *Main group Organometallics Optoelectronic Materials and Catalysis lab, Department of Chemistry, National Institute of Technology, Calicut, 673601, India. E-mail: swamy@nitc.ac.in*

[b] *Protein Homeostasis Laboratory, Department of Life Sciences, School of Natural Sciences, Shiv Nadar Institution of Eminence, Delhi-NCR, Gautam Buddha Nagar, Greater Noida, Uttar Pradesh, 201314, India*

the onset and progression of various diseases, including cancer, neurodegenerative disorders, and metabolic syndromes. Despite the development of several viscosity-sensitive rotors targeting LDs,[26] challenges still persist. These include interference from other environmental parameters such as solvent polarity, temperature, and pH, non-specific organelle targeting, poor photostability, and limited accuracy in detecting viscosity changes hinder the precise LD imaging.

Recently, our research focused on designing activatable fluorophores that combine organelle specificity, viscosity sensitivity, and synthetic accessibility. In our previous work, we introduced BODIPY-cyanostilbene-based fluorophores featuring a donor–acceptor (D–A) architecture and demonstrated their ability to localize selectively to LDs and distinguish between cancerous and non-cancerous cells.[27] These molecules exhibited favorable photophysical traits including high brightness, photostability, and sensitivity to viscosity fluctuations. In the present work, our focus is to (1) synthesize new D–A conjugated BODIPY-cyanostilbene fluorophores functionalized with organelle-specific targeting motifs; (2) explore the effect of structural modulations, specifically via tetramethyl substitution on the indacene core; and (3) evaluate the impact of these changes on the optical properties and suitability for bioimaging applications. Here, we tried to build on existing design by incorporating a morpholine group commonly used for lysosomal targeting into two newly synthesized BODIPY-cyanostilbene derivatives. Our findings suggest that hydrophobicity of the target fluorophores rules over the mildly alkaline nature of morpholine functionality, leading to strong and selective accumulation of the probes to LDs. These insights highlight the critical role of hydrophobicity in organelle targeting and could serve as a valuable reference for the future design of efficient organelle-specific probes. The two probes differ in their substitution pattern at the BODIPY core, with one containing sterically demanding tetramethyl groups on the indacene moiety that modulate conformational rigidity and influence the probe's response to environmental viscosity. Detailed spectroscopic analysis and live-cell imaging revealed that both fluorophores exhibit excellent viscosity-dependent fluorescence enhancement, minimal sensitivity to polarity or pH variations, and strong LD specificity. Importantly, they also demonstrate low cytotoxicity and robust imaging performance in live cells, making them suitable candidates for distinguishing two different types of cells.

2. Results and discussion

2.1 Synthesis and characterisation

In this study, we strategically designed and synthesized two fluorescent probes by modifying the molecular conformation through the incorporation of methyl groups on the indacene unit as well as by integrating the organelle-specific functional moiety into the fluorophore. The synthetic routes adopted to synthesize the target fluorophores are shown in Scheme 1 and the detailed synthetic procedure is described in the SI. To summarize, the synthetic strategy involved a stepwise approach,

starting with the synthesis of precursors followed by Suzuki cross-coupling reactions to achieve the desired products. The precursors 1 and 2 were easily synthesized according to the reported methods.[28] Next, the Knoevenagel condensation reaction between compound 2 and 4-bromo phenyl acetonitrile resulted in compound 3, which was then subjected to a palladium-catalyzed Suzuki–Miyaura cross-coupling reaction, leading to the formation of compound 4 in good yields. Furthermore, the BODIPY core precursors (compounds 5 and 6) were synthesized following the reported procedure.[19] Initially, a trifluoroacetic acid (TFA)-catalyzed condensation of 4-bromo benzaldehyde with the corresponding pyrroles resulted in the formation of dipyrromethane intermediates, which were subjected to an oxidation reaction with DDQ (2,3-dichloro-5,6-dicyano-1,4-benzoquinone) to form the respective dipyrromethenes and subsequently these dipyrromethenes underwent complexation with $BF_3 \cdot Et_2O$ in dichloromethane (DCM). Finally, palladium-catalyzed Suzuki–Miyaura cross-coupling reactions of compounds 5 and 6 with the aryl boronic ester (compound 4) resulted in the synthesis of our D–A conjugated morpholine functionalized target fluorophores. All newly synthesized compounds were thoroughly characterized using a range of advanced analytical techniques such as ^1H NMR, ^{13}C NMR, ^{11}B NMR, and ^{19}F NMR spectroscopies, as well as high-resolution mass spectrometry (HRMS) to confirm their structure and purity.

2.2 Photophysical properties

To investigate the optical characteristics of fluorophores 7 and 8, their UV-vis absorption and fluorescence spectra were recorded in DCM. As presented in Fig. 1 and Fig. S18, both compounds exhibit two main absorption bands spanning from 300 to 550 nm. The absorption band near 350 nm is related to the π–π* transition of the cyanostilbene unit, while the band around 500 nm originates from the π–π* ($S_0 \rightarrow S_1$) transition of the BODIPY core. A more detailed overview of these photophysical parameters is provided in Table 1. Distinct spectral differences between the two compounds point to structural influences on their electronic behavior. Compound 7 displays a broadened absorption region between 450 and 480 nm, suggesting some degrees of interaction or overlap between the cyanostilbene and BODIPY units, possibly due to flexible molecular geometry.[27,29,30] In contrast, compound 8, bearing bulky methyl substitutions on the indacene ring, shows well-resolved and sharper absorption bands, implying weaker electronic communication and a more orthogonal orientation between its donor and acceptor units.[27,31] Fluorescence studies with excitation at 350 nm further distinguish the photophysical profiles of the two probes. Compound 7 shows dual emission behavior: a sharp emission band at 523 nm corresponding to the BODIPY core, and a weaker, broader emission that originates from the cyanostilbene unit. This dual emission reflects partial energy transfer, likely due to the flexible meso-aryl rings that allow rotational freedom, thus hindering optimal D–A alignment for efficient transfer.[27,32] On the other hand, compound 8 exhibits a single, intense emission peak at 515 nm, exclusively from the BODIPY unit, with no detectable contribution from the cyanostilbene donor. This clean emission profile suggests complete energy transfer, facilitated by restricted intramolecular motion and better
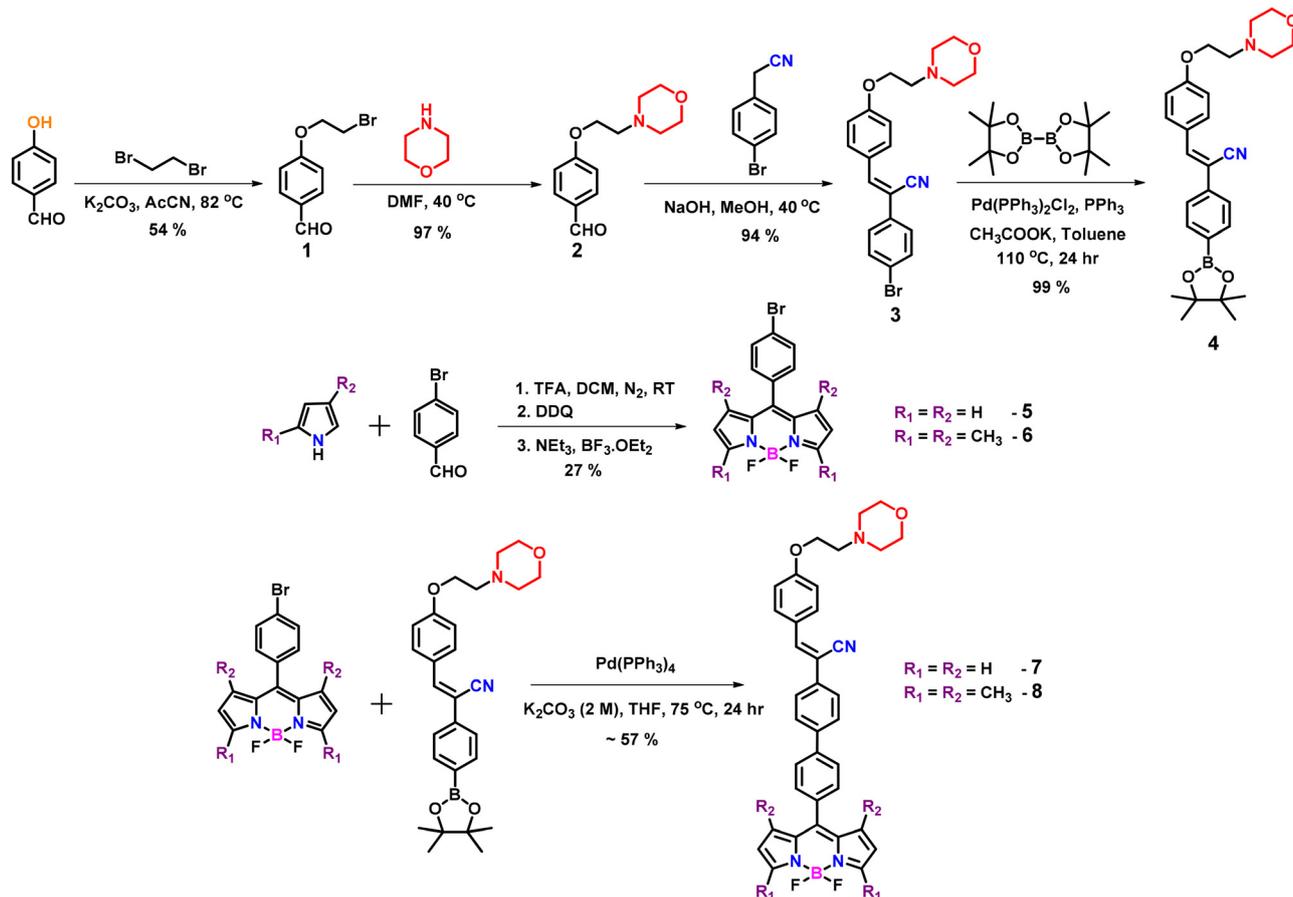
Scheme 1 Synthetic scheme adopted for the target molecules.
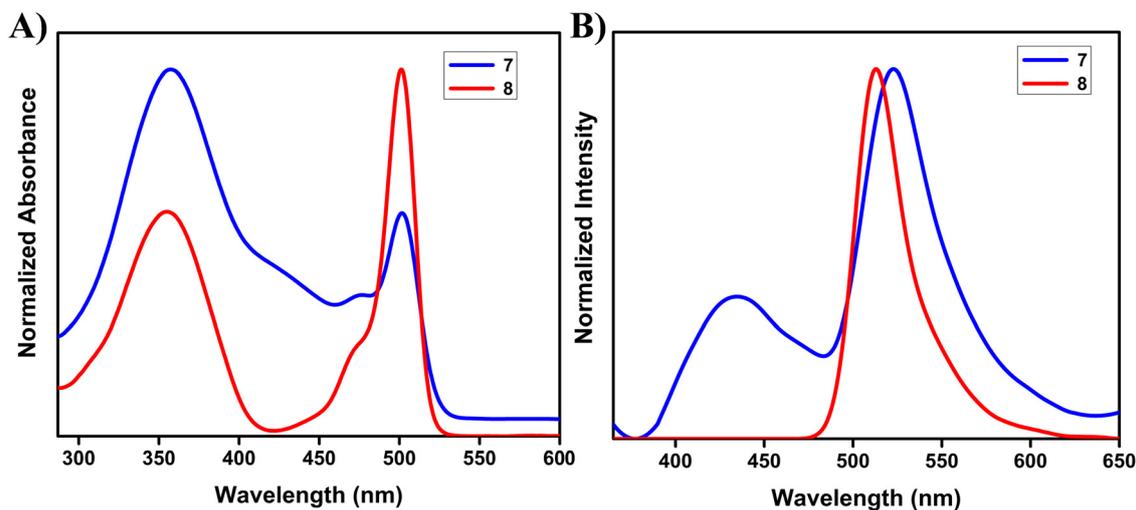
Fig. 1 (A) Normalized absorption (10 μM) and (B) normalized emission spectra of compounds **7** and **8** in DCM (2 μM, λ_{ex} = 350 nm).

orbital alignment owing to steric constraints imposed by the tetramethyl substitutions. The rigidity of compound **8** not only enhances energy transfer efficiency but also suppresses non-radiative decay pathways, resulting in higher fluorescence intensity.[27,33] Supporting these observations, the quantum yield of compound **8** is significantly higher than that of compound **7** (refer to Table 1). Additionally, the emission maximum of compound **7** shows a slight red-shift compared to compound **8**, a feature that likely stems from increased electronic delocalization due to greater planarity and conjugation in the absence of bulky

Table 1 Photophysical data of compounds

Compounds	λ_{abs} (nm)/ε ($\times 10^4$)	λ_{em} (nm)	$\Phi_f{}^a$
7	358 (4), 433 (1.6), 499 (2)	432, 523	16 ± 1
8	356 (2.5), 500 (3.3)	515	55 ± 2

^{a} Quantum yields are calculated using quinine sulfate (0.1 M in H_2SO_4, Φ_F = 57.7%) solution as reference and using the following formula $\phi = \phi_F \times I/I_R \times A_R/A \times \eta^2/\eta_R{}^2$, where ϕ is the quantum yield, I is the integral area of the emission peak, A is the absorbance at λ_{ex}, and η is the refractive index of the solvent.

substituents. These findings underscore the crucial role of molecular design in tuning photophysical behavior. By carefully modulating conformational rigidity and the steric environment, one can fine-tune energy transfer efficiency and fluorescence output, paving the way for the development of highly responsive fluorescent systems.

2.3 Selectivity and competitive studies

Understanding how small-molecule fluorophores behave under biologically relevant conditions is essential for their successful application in cellular imaging. To this end, we evaluated the optical responses of BODIPY-cyanostilbene derivatives (compounds 7 and 8) across a broad range of solvent environments, aiming to determine their sensitivity to polarity as shown in Fig. 2 and Fig. S19 and S20 and Table S1. Initial spectroscopic analysis revealed that both fluorophores display two primary absorption features-one attributed to the cyanostilbene unit (~350 nm) and another from the BODIPY core (~500 nm). Notably, the absorption profiles remained unchanged across solvents of varying polarity (from hexane to DMF), indicating

that the ground-state electronic structure of these molecules is largely unaffected by a solvent dielectric constant.[27,31] Emission behavior, however, revealed subtle but clear distinctions. While the emission maxima of both compounds were relatively consistent across solvents, compound 7 exhibited noticeable changes in emission intensity depending on the polarity of the medium. In polar solvents, the cyanostilbene donor emission was quenched significantly, implying an enhanced intramolecular energy transfer to the BODIPY acceptor. In non-polar solvents, the donor emission was more prominent, suggesting reduced energy transfer efficiency. In contrast, compound 8 displayed a single dominant emission band from the BODIPY unit, regardless of the solvent environment, likely due to the restricted molecular motion imposed by its tetramethyl-substituted core. Given the molecular design of these probes, we next examined their response to viscosity, a crucial parameter for mapping lipid-rich organelles such as LDs. In a viscous glycerol medium, compound 7 showed a marked increase in fluorescence intensity, consistent with molecular rotor behavior where restricted intramolecular rotation suppresses non-radiative relaxation pathways. Compound 8, lacking such flexibility, exhibited only marginal fluorescence enhancement, confirming that structural rigidity hinders viscosity sensitivity.

To determine their biological specificity, both compounds were tested in the presence of a wide spectrum of physiologically relevant ions, amino acids, and reactive species as illustrated in Fig. 2 and Fig. S21. These included metal ions (e.g., Fe^{3+}, Zn^{2+}, and Cu^{2+}), small anions (e.g., NO_2^- and HCO_3^-), reactive oxygen/sulfur species (e.g., H_2O_2, GSH, and Cys), and polar amino acids. Impressively, the fluorescence profiles of both probes remained largely unaltered, suggesting excellent
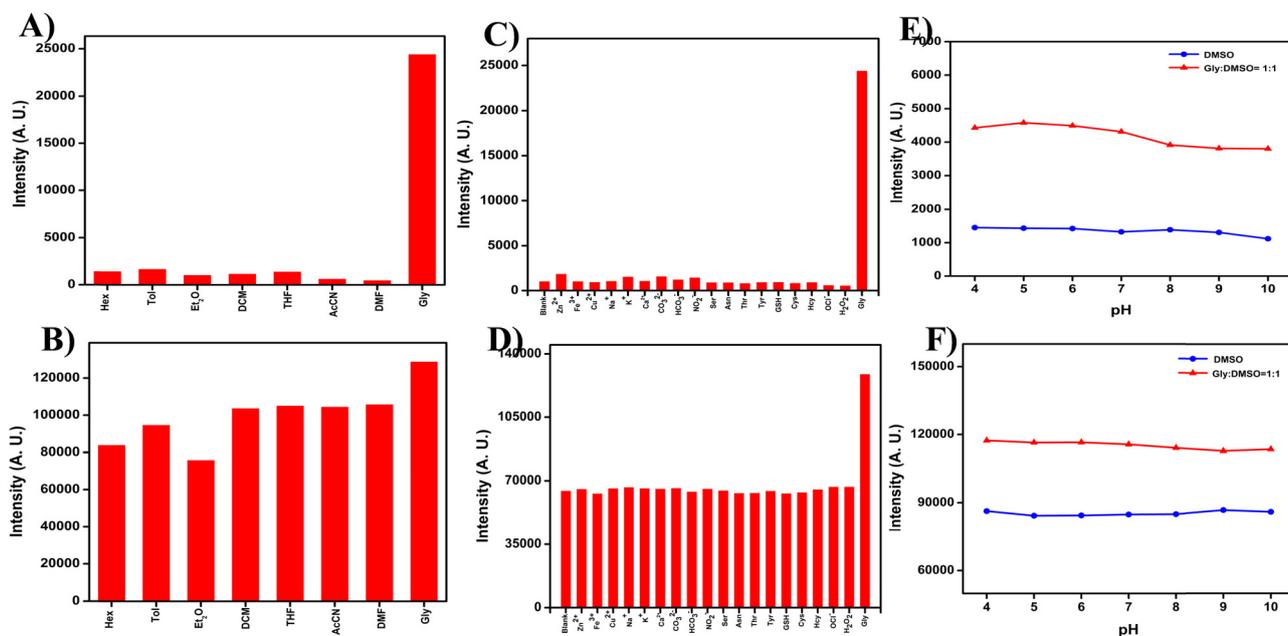

Fig. 2 Emission studies of compounds (A) 7 and (B) 8 in different solvent polarity. Emission spectra of compounds (C) 7 and (D) 8 in DMSO with various competitive species (100 μM) (blank, Zn(OAc)$_2$, FeCl$_3$, Cu(OAc)$_2$, NaCl, KCl, CaCl$_2$, K$_2$CO$_3$, NaHCO$_3$, NaNO$_2$, Ser, Asn, Thr, Tyr, GSH, Cys, Hcy, OCl$^-$, H$_2$O$_2$, and glycerol). Emission studies of compounds (E) 7 and (F) 8 at different pH values and viscous media (DMSO and DMSO : glycerol = 1 : 1) (2 μM, λ_{ex} = 350 nm).

chemical selectivity toward viscosity changes rather than interference from these species. We further investigated the impact of pH variation, a parameter that varies widely between cellular compartments and disease states. The fluorescence of both compounds remained stable over a physiological pH range (4–10), under both low-viscosity (DMSO) and high-viscosity (glycerol : DMSO 1 : 1) conditions (see Fig. 2 and Fig. S22).[34] This reinforces the pH-independence of their photophysical behavior, a valuable trait for biological applications where local acidity may fluctuate. Furthermore, in order to investigate the stability of our target compounds, we monitored their fluorescence behavior in DMSO upon treatment with 10 equivalents of trifluoroacetic acid (TFA) over a 24 h. As shown in Fig. S23, the emission spectra of both probes exhibited a marked increase in fluorescence intensity immediately after TFA addition, which remained consistent over time. This might be attributed due to protonation of the tertiary amine in the morpholine moiety of our probes, which effectively suppresses the photoinduced electron transfer (PET) from the morpholine nitrogen to the BODIPY core leading to a significant increase in emission intensity. For compound **8**, a slight decrease in intensity was observed after 6 h. However, the fluorescence intensity remained substantially higher than the compound **8** without TFA. These findings indicate that the BODIPY framework retains its structural integrity under acidic conditions, with no signs of BF$_2$ dissociation or

decomposition of the pyrrolic core.[35] We have also evaluated the impact of aggregation on our fluorophores *via* fluorescence emission studies in DMSO–water mixtures. As depicted in Fig. S24, both probes exhibited a significant decrease in fluorescence intensity with increasing water content (0–90%), a characteristic behavior of aggregation-caused quenching (ACQ). These results confirm that the fluorescence response of the probes arises specifically from viscosity variations rather than aggregate formation. Altogether, these findings establish compounds **7** and **8** as robust, selective, and viscosity-sensitive probes, capable of operating effectively in complex biological environments without interference from pH, polarity, or common intracellular species.

2.4 Viscosity sensitivity measurements

To systematically evaluate how microenvironmental parameters such as viscosity influences the photophysical properties of our BODIPY-cyanostilbene fluorophores, we conducted fluorescence studies across a dynamic viscosity range from 2 cP (pure DMSO) to 878.32 cP (glycerol) by varying the DMSO/glycerol ratio as shown in Fig. 3. Compound **7**, when excited at 350 nm, exhibited very weak fluorescence in pure DMSO, a low-viscosity environment due to intramolecular rotations, which facilitates non-radiative deactivation of the excited state. However, as the glycerol content increased, a remarkable enhancement in emission intensity was observed, resulting in a ∼24-fold increment in

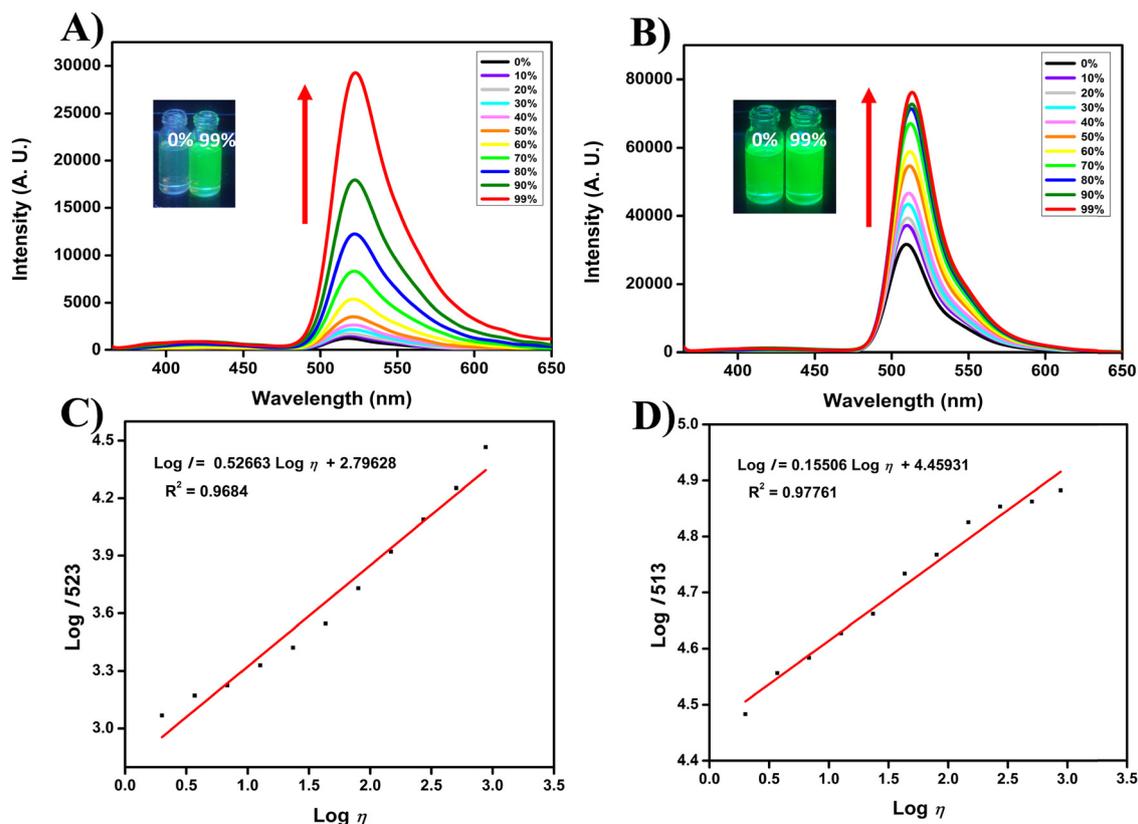**Fig. 3** Emission spectra of compounds (A) **7** (10 μM, λ_{ex} = 350 nm) and (B) **8** (1 μM, λ_{ex} = 350 nm), recorded in DMSO−glycerol mixtures with increasing glycerol content from 0% to 99%. Photographs captured under a UV 365 nm lamp are shown above each spectrum. Graphs illustrate the linear relationship between log *I* (fluorescence intensity) and log η (viscosity) of compounds **7** (C) and **8** (D).

nearly pure glycerol (99%). This fluorescence amplification is attributed to the suppression of intramolecular rotation in a viscous medium, which inhibits non-radiative decay and promotes radiative relaxation. This behavior is characteristic of a molecular rotor mechanism, confirming that compound **7** is highly sensitive to local viscosity changes. In contrast, compound **8** displayed only a modest ~2-fold fluorescence enhancement across the same viscosity gradient. This can be rationalized by its structural rigidity; the presence of four methyl substituents at the indacene core restricts torsional freedom even under low-viscosity conditions, thereby limiting further fluorescence modulation by viscosity.[36] As a result, compound **8** exhibits relatively stable emission intensity, which is less responsive to environmental viscosity but beneficial for applications requiring consistent signal output.

To quantitatively assess viscosity sensitivity, we analyzed the fluorescence data using the Förster–Hoffmann equation:[27,37]

$$\log I = C + x \log \eta \qquad (1)$$

where I stands for the fluorescence intensity, C is a constant, x reflects the probe's sensitivity to viscosity, and η is the viscosity. Compound **7** exhibited a significantly higher slope (x value), reinforcing its superior sensitivity to viscosity and confirming its molecular rotor functionality compared to compound **8** as shown in Fig. 3.

2.5 Theoretical calculations

To achieve a comprehensive understanding of the structural and electronic factors underlying the distinct photophysical characteristics of our target fluorophores, we employed density functional theory (DFT) calculations using the Gaussian 09W suite. All calculations were carried out in the gas phase at the B3LYP/6-31G(d,p) level of theory, without applying symmetry constraints.[27,38] Our primary focus was to analyze the dihedral

angles between the BODIPY core and the *meso*-substituted phenyl ring, which play a pivotal role in modulating the electronic coupling between the BODIPY and cyanostilbene chromophores (Fig. S25). One of the primary structural distinctions between compound **7** and **8** lies in the torsional relationship between the BODIPY framework and the *meso*-phenyl substituent. Geometry optimization revealed that compound **7** maintains a tilted conformation with a dihedral angle of ~53°, allowing partial π-conjugation across the chromophores. In contrast, compound **8** adopts a nearly orthogonal geometry (~90°), which disrupts π-conjugation and minimizes electronic communication between the donor and acceptor units thereby enabling efficient and complete energy transfer from the donor to the acceptor. This divergence in conformation plays a pivotal role in shaping their photophysical attributes. In compound **7**, the semi-planar alignment fosters moderate orbital overlap which facilitates partial intramolecular charge transfer resulting in dual-band fluorescence. Conversely, the rigid perpendicular alignment in compound **8** eliminates such interactions, resulting in a highly localized excitation and a single emission pathway. To further understand these electronic features, we analyzed the frontier molecular orbitals (FMOs) of both molecules as shown in Fig. 4 and Table S2. In compound **7**, the HOMO and LUMO+1 were largely localized on the cyanostilbene moiety, while the LUMO and HOMO−1 were confined to the BODIPY unit. Interestingly, the partial delocalization observed in the LUMO and LUMO+1 orbitals support the interchromophoric communication consistent with energy transfer mechanisms. On the other hand, compound **8** displayed a more compartmentalized orbital distribution: both the HOMO and the LUMO are centered on the BODIPY core, while HOMO−1 and LUMO+1 are localized on the cyanostilbene unit, with no evidence of orbital overlap or interaction. This electronic isolation confirms the orthogonality of the chromophores and supports the absence of energy transfer, as observed in experimental emission studies.
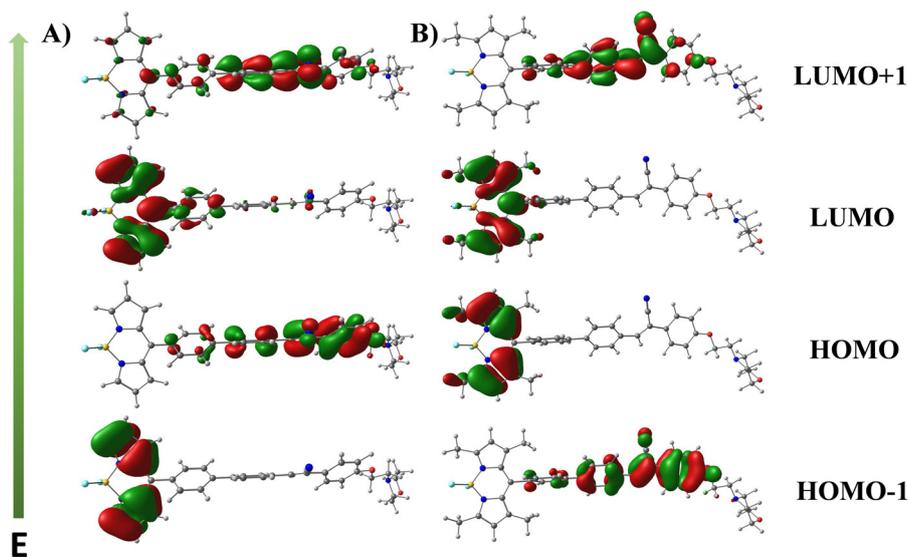

Fig. 4 Important frontier molecular orbitals (MOs) of compounds **7** (A), and **8** (B). Calculations were based on the optimized ground state geometry at the B3LYP/6-31G(d,p) level with Gaussian 09.

To validate the absorption behavior and observed experimental trends, we employed time-dependent DFT (TD-DFT) calculations on the ground-state optimized structures (see Fig. S26 and Table S3). The computed vertical excitation energies corresponded well with experimental UV-vis spectra. For compound 7, the principal transitions involved HOMO → LUMO+1 and HOMO−1 → LUMO, representing excitations centered on the cyanostilbene and BODIPY fragments, respectively. The broader absorption band observed in compound 7 is likely due to partial orbital interactions between the two chromophores. In contrast, compound 8 exhibited distinct and well-separated transitions: HOMO−1 → LUMO+1 and HOMO → LUMO, corresponding to the isolated excitations within the cyanostilbene and BODIPY domains, respectively. This accounts for the additive nature of its absorption features, as seen experimentally. Overall, these computational insights highlight how subtle changes in molecular geometry and orbital distribution can profoundly impact the photophysical response of D–A systems.

2.6 Lipid droplet localization

After analyzing the promising features of our target fluorophores, we next evaluated their biological applicability. Cytotoxicity assessment is a crucial prerequisite before undertaking detailed biological studies. Therefore, we conducted cytotoxicity tests using the 3-[4,5-dimethylthiazol-2-yl]-2,5-diphenyltetrazolium bromide (MTT) assay on HeLa cells as shown in Fig. S27. Cells were treated with increasing concentrations of the fluorophores for 24 hours. The results showed that cell viability remained above 50% even at concentrations up to 5 μM, although viability gradually decreased at higher concentrations. This is well within the acceptable range for further studies, as the effective concentration required for cellular imaging was approximately 500 nM, minimizing any concerns regarding toxicity, consistent with our previous findings.[27]

Moving forward, we investigated the co-localization behaviour of our probes with cellular organelles. Based on our previous studies with similar BODIPY-cyanostilbene fluorophores, which showed LD localization, we sought to modify the current fluorophores with an organelle-targeting group. With this aim, we introduced a morpholine moiety, known for their lysosomal localization. We anticipated that the probes would either localize specifically to lysosomes or simultaneously target both lysosomes and LDs, allowing us to visualize and monitor the dynamic interplay between these organelles. However, as evidenced by the appearance of bright, punctate fluorescent spots distributed throughout the cytoplasm, these probes specifically localized to LDs.[39,40] To confirm LD-specific targeting, we performed co-localization studies using the commercial LD marker Nile red in HeLa cells as illustrated in Fig. 5 and Fig. S28. The complete spectral overlap between the green emission of our probes and the red fluorescence of Nile red confirmed their selective accumulation in LDs and the Pearson coefficient was calculated to be 0.96 and 0.98 for compounds 7 and 8, respectively. Furthermore, co-localization experiments with other organelle-specific dyes, including Lyso-Tracker red (lysosomes) and Hoechst (nuclei), were also performed to validate the specificity as shown in Fig. S29 and S30. No significant spectral overlap was observed between the fluorophores and the organelle-specific trackers, further confirming the LD specificity of our probes. This is likely attributed to the strong lipophilicity arising from the highly conjugated aromatic structure of our probes outweighs the mildly alkaline character of the morpholine moiety.[26] These results emphasise the crucial role of hydrophobicity in organelle targeting and can help guide the design of more effective probes in future studies. Additionally, we evaluated the photostability of our probes, a fundamental requirement for advanced clinical applications. The fluorescence intensity remained stable over an extended period, validating the good photostability of our probes (Fig. S31). In summary, our probes specifically localize to LDs and exhibit low cytotoxicity, good photostability, and resistance to interference from competitive biological species.

2.7 Tracking LD changes during oleic acid (OA) treatment

To evaluate the efficacy of our target compounds in monitoring changes in the LD production, HeLa cells were pre-treated with OA for 30 minutes, followed by incubation with the compounds
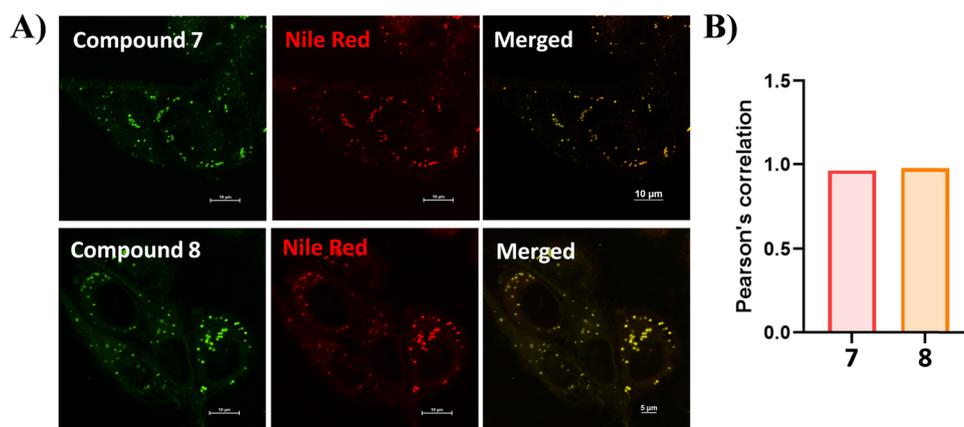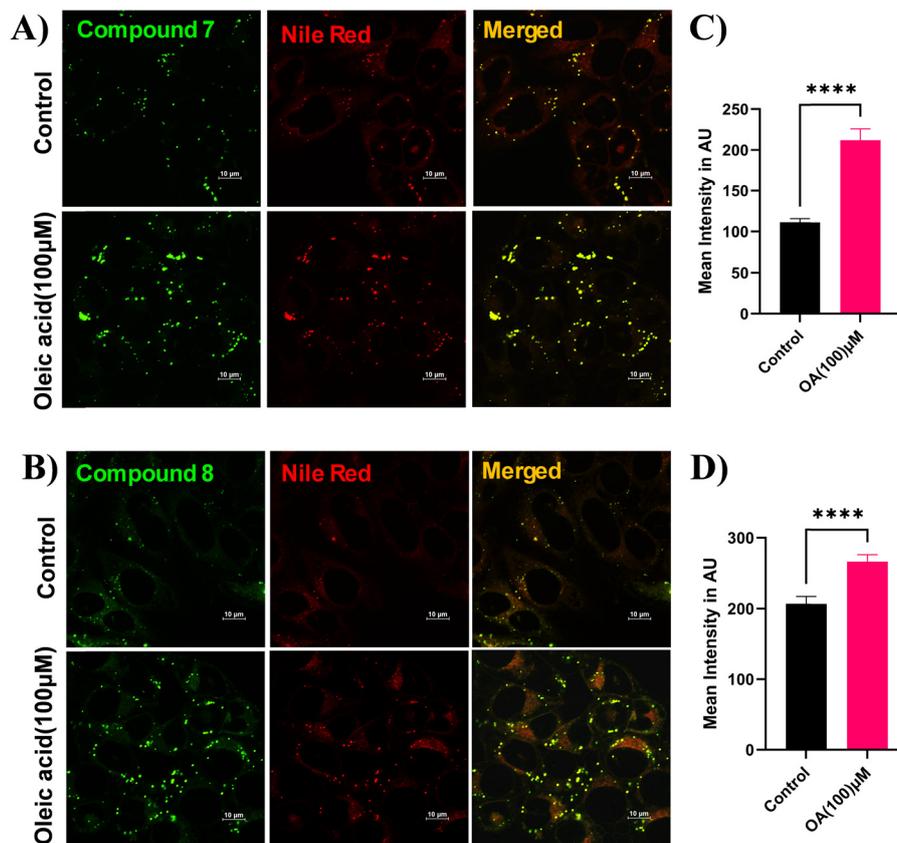

Fig. 5 Confocal fluorescence microscopy images showing intracellular co-localization in HeLa cells. Cells were treated with compounds 7 and 8 (500 nM) (left), commercially available lipid droplet staining Nile red (middle), and the merged images (right). (B) Pearson's correlation coefficient quantifying the extent of co-localization between compounds 7 and 8 and Nile red.

Fig. 6 Confocal fluorescence microscopy images of HeLa cells incubated with 0 μM (control) and 100 μM OA for 30 minutes followed by staining with compounds **7** (A) and **8** (B) (500 nM) (left), commercially available lipid droplet staining Nile red (middle), and the merged images (right). Quantitative comparison of relative fluorescence intensities for compounds **7** (C) and **8** (D), respectively.

for an additional 30 minutes. OA, due to its nutrient-rich nature and efficient cellular uptake, stimulates the production of additional LDs to accommodate excess lipid storage.[41] As shown in Fig. 6, the probes exhibited very weak fluorescence in the absence of OA. In contrast, treatment with 100 μM OA resulted in a significant enhancement of fluorescence intensity, corresponding to an increased number of LDs. These findings demonstrate the potential of our probes to visualize and quantify OA-induced alterations in LD abundance *via* fluorescence intensity modulation.

2.8 Discriminating normal and cancer cells

Due to their uncontrolled division and rapid growth, cancer cells have higher metabolic demands, leading to a greater number and larger size of LDs with increased viscosity compared to normal cells. Based on this, we were curious to determine whether our probes could serve as biomarkers to distinguish normal from cancerous cells. To test this, we incubated the probes with two different cell lines: HeLa cells (cancer model) and HEK293T cells (normal model) and performed fluorescence imaging under identical conditions using confocal microscopy. As shown in Fig. 7, a clear distinction was observed between the two cell types: HeLa cells exhibited markedly stronger fluorescence, likely due to the combined effects of increased LD number and higher

LD viscosity, whereas HEK293T cells displayed weak fluorescence and fewer LDs. Quantitative analysis further confirmed this difference, with compound **7** showing a 2.6-fold increase and for compound **8** showing a 1.9-fold increment in fluorescence intensity in HeLa cells compared to HEK293T cells. These results demonstrate that our probes are promising candidates for distinguishing cancerous cells from healthy cells.

3. Conclusions

In this study, we successfully synthesized two new D–A conjugated fluorophores based on BODIPY-cyanostilbene scaffolds which can exclusively localize to LDs. Despite their structural similarity, a subtle but critical difference in their molecular conformations led to markedly distinct photophysical behaviors. Compound **7** exhibited weak fluorescence in low-viscosity environments, primarily due to the free intramolecular rotation of the *meso*-phenyl rings, which facilitates non-radiative decay of the excited state. However, as the viscosity of the surrounding medium increased from 0% to 99% glycerol content, a dramatic 24-fold enhancement in emission intensity was observed. This strong viscosity-dependent fluorescence response identified compound **7** as an efficient molecular rotor. In contrast, compound **8**, which bears four methyl substituents on the indacene
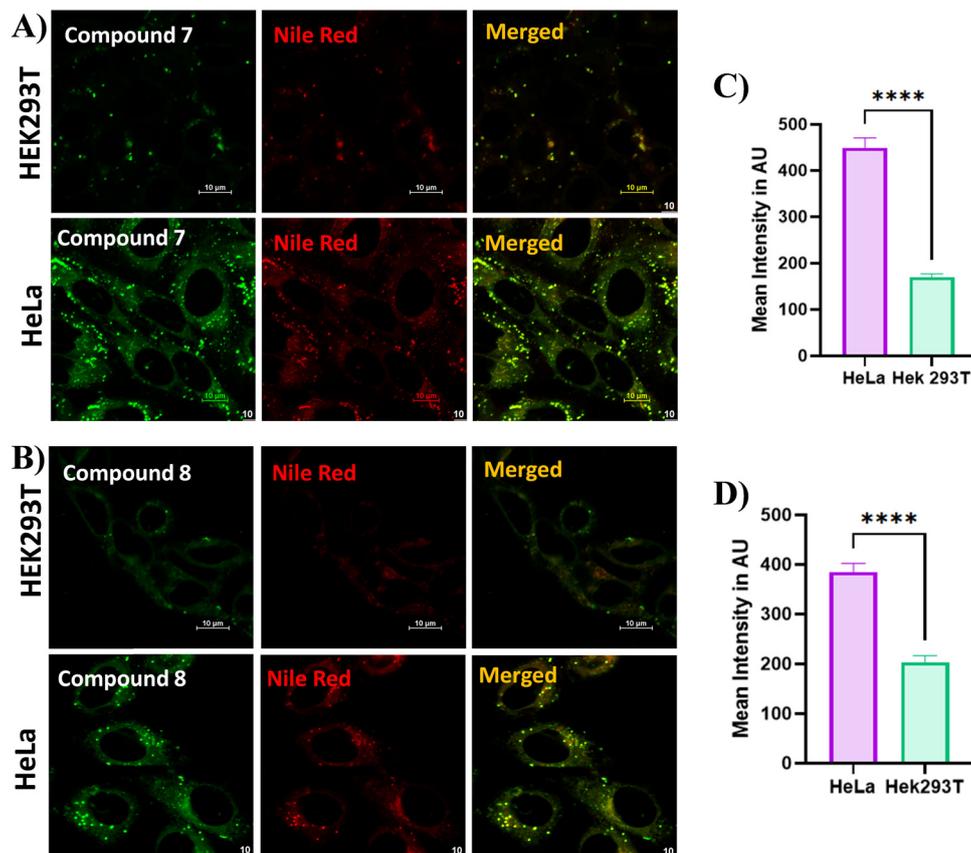
Fig. 7 Confocal fluorescence microscopy images showing different cell lines treated with compounds **7** (A) and **8** (B) (500 nM) (left), commercially available lipid droplet staining Nile red (middle), and the merged images (right) including normal cells (HEK293T) and cancer cells (HeLa). Quantitative comparison of fluorescence intensities for compounds **7** (C) and **8** (D) in cancer cells and normal cells, respectively.

core, possessed a more rigid molecular structure that limits intramolecular motion. As a result, it exhibited strong fluorescence even in low-viscosity media, with only minimal intensity enhancement under viscous conditions. The distinct optical properties of both compounds were further supported by DFT and TD-DFT calculations. The computational studies provided insights into the conformational geometries, electronic distributions, and excited-state transitions, all of which align well with the experimental observations and further reinforce the role of structural rigidity in modulating fluorescence behaviour. Furthermore, both compounds selectively localized in LDs, suggesting that overall lipophilicity rather than the moderate alkalinity of the morpholine moiety predominantly governs their subcellular distribution. The results underscore the significant role that hydrophobicity plays in directing organelle specificity and can guide the design of more effective probes in future studies. Additionally, both fluorophores exhibited good photostability, low cytotoxicity, and the capability to discriminate between normal and cancerous cells.

Conflicts of interest

The authors declare no conflicts of interest.

Data availability

The data that support the findings of this study are available in the SI of this article. The data that support the findings of this study are available in the supplementary material of this article which includes ^{1}H NMR, ^{13}C NMR, HRMS characterization data for all the compounds, photophysical data, bioimaging results-cytotoxicity, co-localization, photostability, and DFT data. See DOI: **https://doi.org/10.1039/d5nj02328a**

Acknowledgements

References

1 H. Sung, J. Ferlay, R. L. Siegel, M. Laversanne, I. Soerjomataram, A. Jemal and F. Bray, *CA Cancer J. Clin.*, 2021, **71**, 209–249.

2 B. Liu, H. Zhou, L. Tan, K. T. H. Siu and X.-Y. Guan, *Sig Transduct Target Ther.*, 2024, **9**, 175.

3 (*a*) H. Zhu, J. Fan, J. Dua and X. Peng, *Acc. Chem. Res.*, 2016, **49**, 2115–2126; (*b*) Y. Zhao, W. Shi, X. Li and H. Ma, *Chem. Commun.*, 2022, **58**, 1495–1509; (*c*) H. Tian, A. C. Sedwick, H.-H. Han, S. Sen, G.-R. Chen, Y. Zang, J. L. Sessler, T. D. James, J. Li and X.-P. He, *Coord. Chem. Rev.*, 2021, **427**, 213577–213591.

4 R. V. J. Farese and T. C. Walther, *Cell*, 2009, **139**, 855–860.

5 (*a*) M. Gao, X. Huang, B.-L. Song and H. Yang, *Prog. Lipid Res.*, 2019, **75**, 100989–100999; (*b*) M. F. Renne and H. Hariri, *front. Cell Dev. Biol.*, 2021, **9**, 726261–726271; (*c*) Y. Jin, Y. Tan, J. Wu and Z. Ren, *Cell Death Discov.*, 2023, **9**, 254–262; (*d*) J. Z. Hsia, D. Liu, L. Haynes, R. Cruz-Cosme and Q. Tang, *Microorganisms*, 2024, **12**, 647–670.

6 (*a*) A. L. S. Cruz, E. A. Barreto, N. P. B. Fazolini, J. P. B. Viola and P. T. Bozza, *Cell Death Dis.*, 2020, **11**, 105–120; (*b*) R. Munir, J. Lisec, J. V. Swinnen and N. Zaidi, *Br. J. Cancer*, 2019, **120**, 1090–1098.

7 J. A. Olzmann and P. Carvalho, *Nat. Rev. Mol. Cell Biol.*, 2019, **20**, 137–155.

8 A. Zadoorian, X. Du and H. Yang, *Nat. Rev. Endocrinol.*, 2023, **19**, 443–459.

9 (*a*) F. Geltinger, L. Schartel, M. Wiederstein, J. Tevini, E. Aigner, T. K. Felder and M. Rinnerthaler, *Molecules*, 2020, **25**, 5053–5083; (*b*) E. Jarc and T. Petan, *Yale J. Biol. Med.*, 2019, **92**, 435–452.

10 B. C. Farmer, A. E. Walsh, J. C. Kluemper and L. A. Johnson, *Front. Neurosci.*, 2020, **14**, 742–754.

11 D. Delmas, A. K. Cotte, J.-L. Connat, F. Hermetet, F. Bouyer and V. Aires, *Cancers*, 2023, **15**, 4100–4116.

12 P. Greenspan, E. P. Mayer and S. D. Fowler, *J. Cell Biol*, 1985, **100**, 965–973.

13 A. Tabero, F. García-Garrido, A. Prieto-Castañeda, E. Palao, A. R. Agarrabeitia, I. García-Moreno, A. Villanueva, S. de la Moya and M. J. Ortiz, *Chem. Commun.*, 2020, **56**, 940–943.

14 (*a*) G. Jiang, Y. Jin, M. Li, H. Wang, M. Xiong, W. Zeng, H. Yuan, C. Liu, Z. Ren and C. Liu, *Anal. Chem.*, 2020, **92**, 10342–10349; (*b*) L. Guo, M. Tian, Z. Zhang, Q. Lu, Z. Liu, G. Niu and X. Yu, *J. Am. Chem. Soc.*, 2021, **143**, 3169–3179.

15 Y. Tatenaka, H. Kato, M. Ishiyama, K. Sasamoto, M. Shiga, H. Nishitoh and Y. Ueno, *Biochemistry*, 2019, **58**, 499–503.

16 (*a*) K.-N. Wang, L.-Y. Liu, D. Mao, S. Xu, C.-P. Tan, Q. Cao, Z.-W. Mao and B. Liu, *Angew. Chem., Int. Ed.*, 2021, **60**, 15095–15100; (*b*) Y. Chen, X.-R. Wei, R. Sun, Y.-J. Xu and J.-F. Ge, *Org. Biomol. Chem.*, 2018, **16**, 7619–7625; (*c*) M. Tian, E. Ge, B. Dong, Y. Zuo, Y. Zhao and W. Lin, *Anal. Chem.*, 2021, **93**, 3602–3610; (*d*) X. Li, C. Long, Y. Cui, F. Tao, X. Yu and W. Lin, *ACS Sens.*, 2021, **6**, 1595–1603; (*e*) T. Yoshihara,

R. Maruyama, S. Shiozaki, K. Yamamoto, S.-I. Kato, Y. Nakamura and S. Tobita, *Anal. Chem.*, 2020, **92**, 4996–5003; (*f*) F. Meng, J. Niu, H. Zhang, R. Yang, Q. Lu, G. Niu, Z. Liu and X. Yu, *Anal. Chem.*, 2021, **93**, 11729–11735.

17 F. Meng, J. Niu, H. Zhang, R. Yang, Q. Lu, Y. Yu, Z. Liu, G. Niu and X. Yu, *Sens. Actuators, B*, 2021, **329**, 129148–129156.

18 (*a*) N. Zhao, Y. Li, W. Yang, J. Zhuang, Y. Li and N. Li, *Chem. Sci.*, 2019, **10**, 9009–9016; (*b*) L. Shi, K. Li, L.-L. Li, S.-Y. Chen, M.-Y. Li, Q. Zhou, N. Wang and X.-Q. Yu, *Chem. Sci.*, 2018, **9**, 8969–8974; (*c*) S. Li, X. Ling, Y. Lin, A. Qin, M. Gao and B. Z. Tang, *Chem. Sci.*, 2018, **9**, 5730–5735; (*d*) M.-Y. Wu, J.-K. Leung, C. Kam, T. Y. Chou, D. Wang, S. Feng and S. Chen, *Mater. Chem. Front.*, 2021, **5**, 3043–3049; (*e*) F. Zhang, Y. Liu, B. Yang, G. Wen and B. Liu, *Sens. Actuators, B*, 2020, **322**, 128589–128599.

19 Z. Yang, J. Cao, Y. He, J. H. Yang, T. Kim, X. Peng and J. S. Kim, *Chem. Soc. Rev.*, 2014, **43**, 4563–4602.

20 L. Chao, G. Aodeng, L. Ga and J. Ai, *J. Mol. Struct.*, 2024, **1322**, 140617–140638.

21 X. Zhang, S. Li, H. Ma and H. Wang, *Theranostics*, 2022, **12**, 3345–3371.

22 J. Yin, L. Huang, L. Wu, J. Li, T. D. James and W. Lin, *Chem. Soc. Rev.*, 2021, **50**, 12098–12150.

23 M. K. Kuimova, S. W. Botchway, A. W. Parker, M. Balaz, H. A. Collins, H. L. Anderson, K. Suhling and P. R. Ogilby, *Nat. Chem.*, 2009, **1**, 69–73.

24 K. Bera, A. Kiepas, I. Godet, Y. Li, P. Mehta, B. Ifemembi, C. D. Paul, A. Sen, S. A. Serra, K. Stoletov, J. Tao, G. Shatkin, S. J. Lee, Y. Zhang, A. Boen, P. Mistriotis, D. M. Gilkes, J. D. Lewis, C.-M. Fan, A. P. Feinberg, M. A. Valverde, S. X. Sun and K. Konstantopoulos, *Nat.*, 2022, **611**, 365–373.

25 H. Xiao, P. Li and B. Tang, *Chem. Eur. J.*, 2021, **27**, 6880–6898.

26 (*a*) K. Li, Y. Wang, Y. Li, W. Shi and J. Yan, *Talanta*, 2024, **227**, 126362–126371; (*b*) G. Li, J. Li, Y. Otsuka, S. Zhang, M. Takahashi and K. Yamada, *Materials*, 2020, **13**, 677–686; (*c*) R. Žvirblis, K. Maleckaitė, J. Dodonova-Vaitkūnienė, D. Jurgutis, R. Žilėnaitė, V. Karabanovas, S. Tumkevičius and A. Vyšniauskas, *J. Mater. Chem. B*, 2023, **11**, 3919–3928; (*d*) M. Olšinová, P. Jurkiewicz, M. Pozník, R. Šachl, T. Prausová, M. Hof, V. Kozmík, F. Teplý, J. Svoboda and M. Cebecauer, *Phys. Chem. Chem. Phys.*, 2014, **16**, 10688–10697; (*e*) J. Zhu, N. K. Tan, K. Kikuchi, A. Kaur and E. J. New, *Anal. Sens.*, 2024, **4**, e202300049; (*f*) J. E. Chambers, M. Kubánková, R. G. Huber, I. López-Duarte, E. Avezov, P. J. Bond, S. J. Marciniak and M. K. Kuimova, *ACS Nano*, 2018, **12**, 4398–4407.

27 C. Kalarikkal, A. Anjali, S. Bhattacharjee, K. Mapa and P. C. A. Swamy, *J. Mater. Chem. B*, 2025, **13**, 1474–1486.

28 (*a*) S. Cao, Y. Xia, J. Shao, B. Guo, Y. Dong, I. A. B. Pijpers, Z. Zhong, F. Meng, L. K. E. A. Abdelmohsen, D. S. Williams and J. C. M. van Hest, *Angew. Chem., Int. Ed.*, 2021, **60**, 17629–17637; (*b*) L. Nagarapu, Aneesa, A. Satyender, G. Chandana and R. Bantu, *J. Heterocycl. Chem.*, 2009, **46**, 195–200.

29 T. Gayathri, A. K. Barui, S. Prashanthi, C. R. Patra and S. P. Singh, *RSC Adv.*, 2014, **4**, 47409–47413.

30 R. P. Nandi, P. C. A. Swamy, P. Dhanalakshmi, S. K. Behera and P. Thilagar, *Inorg. Chem.*, 2021, **60**, 5452–5462.

31 P. C. A. Swamy, S. Mukherjee and P. Thilagar, *Inorg. Chem.*, 2014, **53**, 4813–4823.

32 P. C. A. Swamy, S. Mukherjee and P. Thilagar, *Chem. Commun.*, 2013, **49**, 993–995.

33 (*a*) A. Loudet and K. Burgess, *Chem. Rev.*, 2007, **107**, 4891–4932; (*b*) G. Ulrich, R. Ziessel and A. Harriman, *Angew. Chem., Int. Ed.*, 2008, **47**, 1184–1201.

34 Y. Wu, W. Shu, C. Zeng, B. Guo, J. Shi, J. Jing and X. Zhang, *Dyes Pigm.*, 2019, **168**, 134–139.

35 (*a*) M. Wang, M. G. H. Vicente, D. Mason and P. Bobadova-Parvanova, *ACS Omega*, 2018, **3**, 5502–5510; (*b*) T. Stemler, C. Hoffmann, I. M. Hierlmeier, S. Maus, E. Krause, S. Ezziddin, G. Jung and M. D. Bartholomä, *ChemMedChem*, 2021, **16**, 2535–2545.

36 (*a*) Y. Zhang, Z. Li, W. Hu and Z. Liu, *Anal. Chem.*, 2019, **91**, 10302–10309; (*b*) L. Zhang, G. Li, H. Zheng and W. Lin, *New J. Chem.*, 2024, **48**, 4565–4569.

37 M. Liu, J. Weng, S. Huang, W. Yin, H. Zhang, Y. Jiang, L. Yang and H. Sun, *Chem. Commun.*, 2023, **59**, 3570–3573.

38 N. Gupta, S. I. Reja, V. Bhalla, M. Gupta, G. Kaur and M. Kumar, *J. Mater. Chem. B*, 2016, **4**, 1968–1977.

39 M. K. Kuimova, G. Yahioglu, J. A. Levitt and K. Suhling, *J. Am. Chem. Soc.*, 2008, **130**, 6672–6673.

40 (*a*) D. Jurgutis, G. Jarockyte, V. Poderys, J. Dodonova-Vaitkuniene, S. Tumkevicius, A. Vysniauskas, R. Rotomskis and V. Karabanovas, *Int. J. Mol. Sci.*, 2022, **23**, 5687–5703; (*b*) C. Caltagirone, M. Arca, A. M. Falchi, V. Lippolis, V. Meli, M. Monduzzi, T. Nylander, A. Rosa, J. Schmidt, Y. Talmon and S. Murgia, *RSC Adv.*, 2015, **5**, 23443–23449.

41 (*a*) H. Zheng, G. Li, L. Zhang, M. Fan and W. Lin, *New J. Chem.*, 2024, **48**, 16710–16717; (*b*) D. Wei, Y. Dai, J. Cao and N. Fu, *Anal. Chim. Acta*, 2024, **1299**, 342422; (*c*) X. Wu, X. Wang, Y. Li, F. Kong, K. Xu, L. Li and B. Tang, *Anal. Chem.*, 2022, **94**, 4881–4888.